JOURNAL OF GEOPHYSICAL RESEARCH, VOL. 113, B10305, doi: 10.1029/2007JB005289, 2008

Lower mantle tomography and phase change mapping

Daoyuan Sun[1] and Don Helmberger[1]

Received 23 July 2007; revised 14 June 2008; accepted 3 July 2008; published 7 October 2008.

[1] A lower mantle *S* wave triplication (Scd) has been recognized for many years and appears to be explained by the recently discovered perovskite (PV) to postperovskite (PPV) phase change. Seismic observations of Scd display (1) rapid changes in strength and timing relative to *S* and ScS and (2) early arrivals beneath fast lower mantle regions. While the latter feature can be explained by a Clapeyron slope (γ) of 6 MPa/K and a velocity jump of 1.5% when corrected by tomographic predictions, it does not explain the first feature. Here, we expand on this mapping approach by attempting a new parameterization that requires a sample of D" near the ScS bounce point (δV_S) where the phase height (h_{ph}) and velocity jump (β) are functions of (δV_S). These parameters are determined by modeling dense record sections collected from USArray and PASSCAL data where Grand's tomographic model is the most detailed in D" structure beneath Central America. We also address the range of γ to generate new global models of the phase boundary and associated temperature variation. We conclude that a γ near 9 MPa/K is most satisfactory but requires β to be nonuniform with a range from about 1.0 to 4.0% with some slow region samples requiring the largest values. Moreover, the edges of the supposed buckled slabs delimitated by both *P* and *S* waves display very rapid changes in phase boundary heights producing Scd multipathing. These features can explain the unstable nature of the Scd phase with easy detection to no detection commonly observed. The fine structure at the base of the mantle beneath these edges contains particularly strong reflections indicative of local ultralow velocity zones, which are predicted in some dynamic models.

Citation: Sun, D., and D. Helmberger (2008), Lower mantle tomography and phase change mapping, *J. Geophys. Res.*, *113*, B10305, doi:10.1029/2007JB005289.

1. Introduction

[2] Large-scale structures in the lower mantle derived from numerous tomographic imaging consistently show a belt of high velocity anomalies along the circum-Pacific (Figure 1a). Low velocity anomalies beneath the mid-Pacific and Africa are also well established although with smaller-scale plume-like features which remain controversial [*Anderson*, 2005]. Relatively sharp features have been reported at midmantle depths beneath North America which appear to be slabs [*Grand et al.*, 1997], and many researchers interpret the high-velocity ring (Figure 1a) as slab debris, e.g., review by *Garnero* [2000] and more recently by *van der Hilst* [2004]. The deep earthquakes occurring in the downgoing slabs produce simple isolated body wave phases (*P* and *S*) which can be used to study the smaller-scale features. In particular, secondary arrivals can be seen between *S* and ScS forming a small triplication, roughly 75° to 85° (Figure 2). These arrivals can be commonly observed on recording stations (continental paths) sampling the fast Pacific Ring as first pointed out by *Lay and Helmberger* [1983]. The position of the triplication relative to *S* and ScS appears to vary regionally with the earliest occurring beneath eastern Asia [*Wysession et al.*, 1998]. This depth-dependence of Scd triplications was used to attempt a phase change interpretation by *Sidorin et al.* [1998] in terms of a positive Clapeyron slope. He imposed a velocity discontinuity defined by

$$V'(h) = V(h)\left\{1 + \frac{1}{2}\beta\left[1 + \tanh\left(\frac{1}{w_{ph}} r_{ph}\right)\right]\right\} \qquad (1)$$

where *V(h)* is the original tomographic velocity at the elevation h above the CMB, V' is the new velocity, and β is the amplitude of the velocity jump. The width of the phase transition is w_{ph} which was assumed to be 5 km in Sidorin's efforts based on upper mantle studies. This sharpness produces a clear Scd in synthetics as displayed in Figures 2c and 2d, while a broad transition produces a gradual long-period onset (Figure 2b). A simple break in the velocity gradient (Figure 2a) produces only a long-period diffraction not easily seen at typical periods used in these studies. The r_{ph} in equation (1) is defined by

$$r_{ph}(h) = h_{ph} - h - \frac{\gamma}{\rho(h)}\Delta T(h). \qquad (2)$$

[1]Seismological Laboratory, California Institute of Technology, Pasadena, California, USA.

0148-0227/08/2007JB005289$09.00

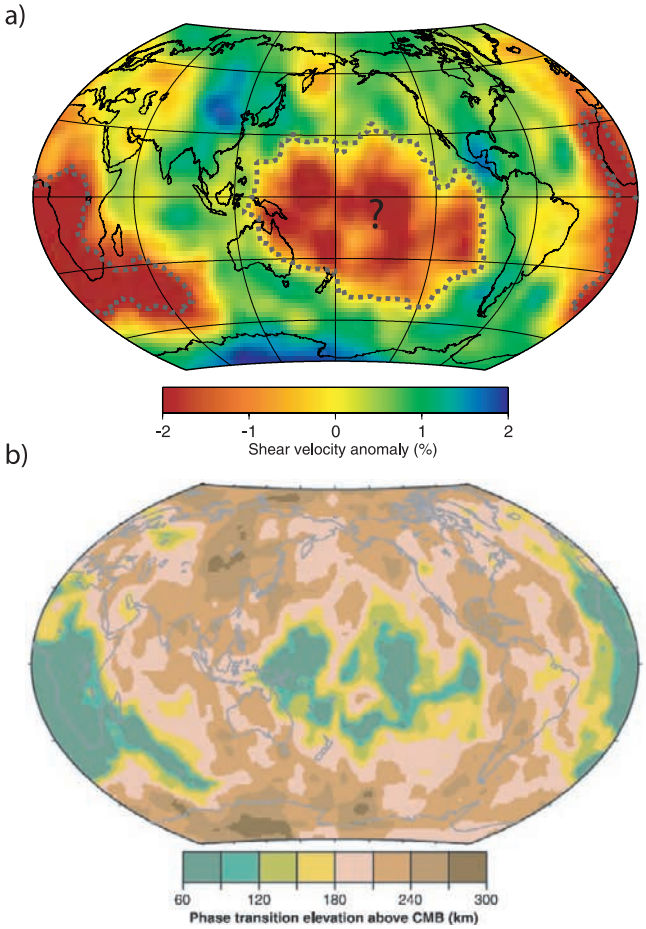

Figure 1. Display of tomographic results from *Grand* [2002] along with possible mapping into thickness of a proposed post-perovskite layer at the CMB. (a) The bottom 240 km layer variation in shear wave velocity. (b) A map of a possible phase boundary discontinuity constructed from Figure 1a assuming that temperature can be deduced from these shear velocity variations (δVs) and uniform global chemistry [*Sidorin et al.*, 1999].

where g is the gravitational acceleration in the mantle, $\rho(h)$ is the density at depth h, and $\Delta T(h)$ is the nonadiabatic temperature perturbation which characterizes the temperature dependence of the shear modulus in the mantle [*Sidorin et al.*, 1999]. The phase elevation above CMB for the reference 1-D model is defined by h_{ph} where the velocity jump occurs. Thus, only three parameters were needed to perform the mapping (Figure 1b), namely, β, h_{ph}, and γ. *Sidorin et al.* [1999] calibrated this model to the Scd triplication data by matching the differential times (Scd–S) for various regions around the circum-Pacific. A 2-D synthetic for each source-station pair was used to determine the h_{ph} and γ for each region following a least squares modeling procedure. The velocity jump β = 1.5% was assumed as the smallest possible jump to explain Scd in fast regions and thus help to explain the few values reported beneath warm regions [*Wysession et al.*, 1998]. To preserve the ScS-S differential times used in deriving Grand's model, *Sidorin et al.* [1999] inserted a low velocity zone just above the CMB as part of the mapping procedure. Synthetics for such 2-D models were generated with a semianalytic code discussed by *Ni et al.* [2000] which has been documented against numerical synthetics by *Ni et al.* [2003].

[3] Two major advances have occurred since this interpretation of the Scd phase data, one in mineral physics and the other in the advance of broadband seismic arrays. The obvious major breakthrough was the direct experimental evidence for a postperovskite phase transition under conditions close to those at the D″ region [*Murakami et al.*, 2004]. Highlights of this discovery have been given by several authors [e.g., *Garnero*, 2004; *Duffy*, 2004]. Numerous studies, both theoretical and experimental, indicates that a phase transition with a positive γ should occur near D″ with a velocity jump between1.5 to 3% but perhaps over a 150 km zone depending on chemistry (e.g., review by *Hirose* [2006]). Does the velocity jump occur abruptly or gradually across the phase change boundary? Although such details are extremely important in interpreting Scd data as evident in Figure 2, they remain largely unknown.

[4] The second issue of modern arrays and their impact on D″ is rapidly becoming apparent as discussed by *Lay and Garnero* [2007]. While *Sidorin et al.* [1999] averaged over regions treating variations as noise to obtain smoothly varying structure, recent studies by *Hutko et al.* [2006], *Sun et al.* [2006], and *Kito et al.* [2007] suggest rapid jumps in the phase boundary height occurring laterally over short-scale lengths of 50 km to 100 km. Are such features caused by buckled slabs since they occur near the edges of sharp structures or are they caused by phase boundary shifts induced by chemical changes or perhaps a combination? The greatly improved station coverage has also allowed better sampling and resolution of P velocity structure. Since the predicted phase change properties for P waves are nearly negligible, such data becomes useful in defining slab debris in D″. In particular, the recent study of differential PKP phases ($PKP_{ab} - PKP_{df}$) strongly supports the detailed tomographic images beneath Central America [*Sun et al.*, 2007a]. Accurate differential times come from measuring the waveform correlation between PKP_{df} and PKP_{ab} which is sensitive to the bottom 500 km of the mantle. PKP_{ab} paths from deep South America earthquakes cross the core-mantle boundary (CMB) beneath Central America indicated by the circles and crosses in Figure 3a. These P velocity values are used to produce the colored tomographic map (Figure 3a) displaying sharp features amazingly similar to Grand's S velocity tomography. Note the slow to fast structure beneath the Cocos Plate with a transition zone less than 300 km wide occurring just off the coast line. There is also a sharp drop in relative correlation between PKP_{df} and PKP_{ab} by over 30% along this same boundary indicative of ultralow velocity zones with small sharp features [*Luo et al.*, 2001]. Combining the S and P wave results yields $R = dlnV_s/dlnV_p$ of about 1.9 which is too low to be produced by temperature alone [*Karato and Karki*, 2001]. The P and S velocity properties for the superplumes proposed earlier by *Masters et al.* [2000] now appears to be well accepted, further confirming the case for changing chemistry.

[5] While Figure 1b predicts weak Scd synthetics when the phase boundary is near the CMB [*Sidorin et al.*, 1998], recent studies identify Scd clearly beneath warm regions as displayed along the lines in Figure 3c [*Lay et al.*, 2006; *He et al.*, 2006; *Sun et al.*, 2007b]. The latter study presents Scd

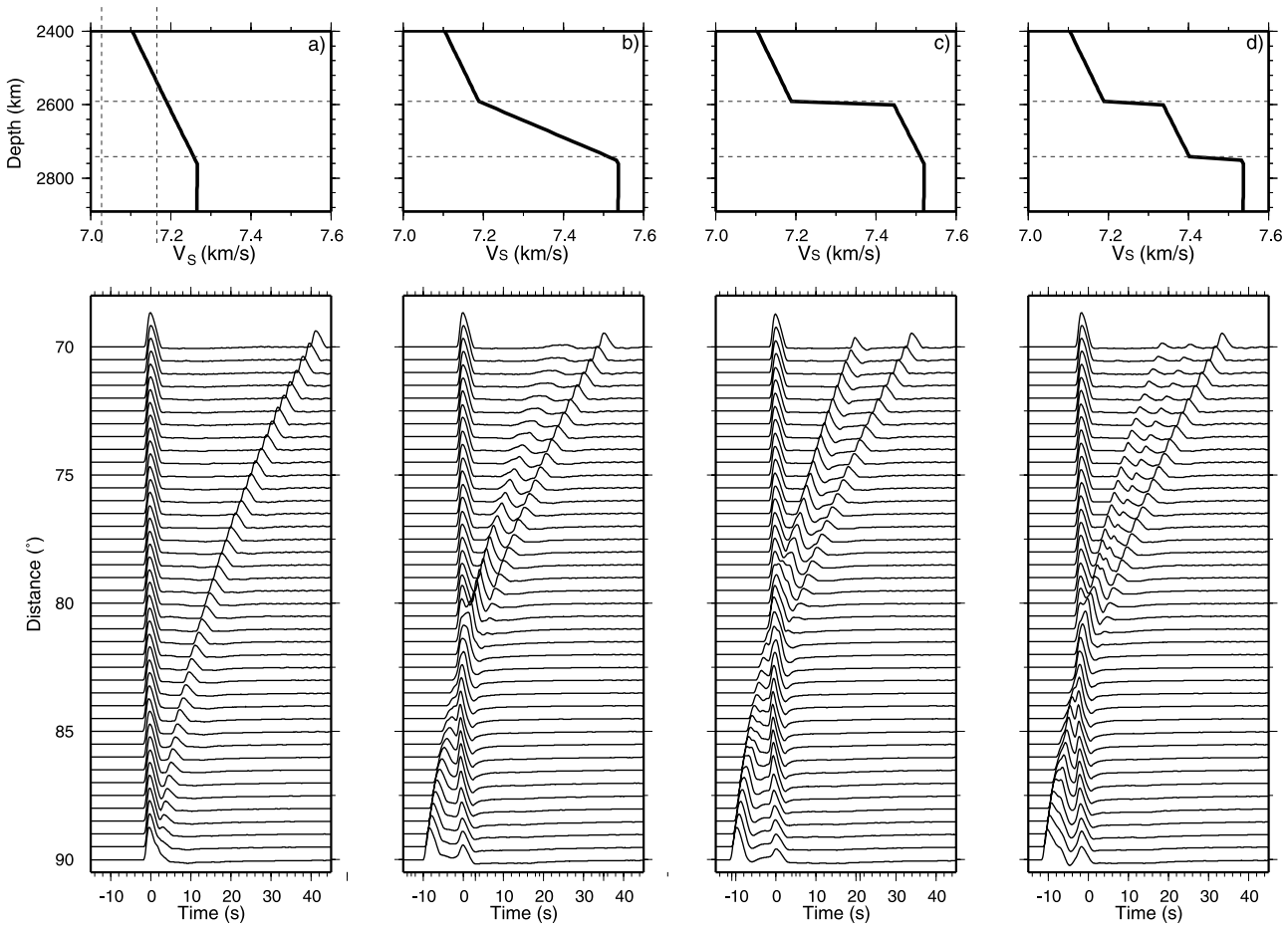

Figure 2. The synthetics for possible 1-D models of D″. (a) The PREM model and the synthetics do not have the Scd phase. (b) A linear velocity gradient and produces the extra Scd phase between *S* and ScS. (c) A sharp velocity jump plus a gradient and (d) two sharp velocity jumps in the model, simulating a complex transition zone.

data sampling beneath the middle of the South African Superplume which is modeled with a velocity jump of 4% occurring 80 km above the CMB. In short, the Sidorin et al. model based on relative travel times needs to be reexamined in terms of waveform modeling of record sections containing Scd detections at several ranges to establish a true triplication with both amplitude and timing information. This is particularly difficult since shallow upper mantle structure and midmantle slabs can alter pulse waveforms [*Song and Helmberger*, 2007]. It appears that stacking high-density observations or detailed waveform modeling can help resolve these issues and provide a clearer picture of the PV to PPV phase boundary and possible change from PPV back to PV near the CMB [*Hernlund et al.*, 2005].

[6] The objective of this paper is to update the Sidorin's effort by developing a new phase boundary mapping tool. To achieve this, we will investigate data sampling beneath Central America, a region well studied as discussed above (earthquake locations are listed in Table 1). Four zones are examined in detail labeled P, A, M, and C in Figure 3b. The first three are relatively pure-path in that they sample a patch of yellow (slightly slow), a slightly fast but nearly PREM beneath the tip of South America, and a fast sample beneath Mexico. The patch C contains a region of rapid Scd changes and is used to add sharpness to our mapping procedure.

2. Calibration of Tomographic Models

[7] In this section, we will follow the basic procedure suggested by *Sidorin et al.* [1999] except we will allow regional variation of γ, h_{ph}, and β. Note that *Sidorin et al.* [1999] found solutions along a rectangular corridor of h_{ph}: γ space running from $2 < \gamma < 12$ MPa/K and $250 < h_{ph} < 150$ km. The best fitting least squares solution is near $h_{ph} = 200$ km and $\gamma = 6$ MPa/K for a uniform global model but γ values as high as 12 MPa/K were accepted. Here, we assume that the velocity perturbation of δV_S in the D" layer is indicative of local dynamics and constitutive state properties. Thus, each sample of Scd in Figure 3b (denoted by P, A, M, C) is assumed to have unique properties in terms of their δV_S averaged over a $2^\circ \times 2^\circ$ grid, and all other samples with the same δV_S will affect the phase boundary the same. To establish that functionality, we determine the best synthetic waveform fits to observe record sections to set $h_{ph}(\delta V_S)$ for a number of values of γ. By matching both arrival times and amplitudes, we were forced to vary β or $\beta(\delta V_S)$. The results are presented in Figure 4 and will be followed by zone-by-

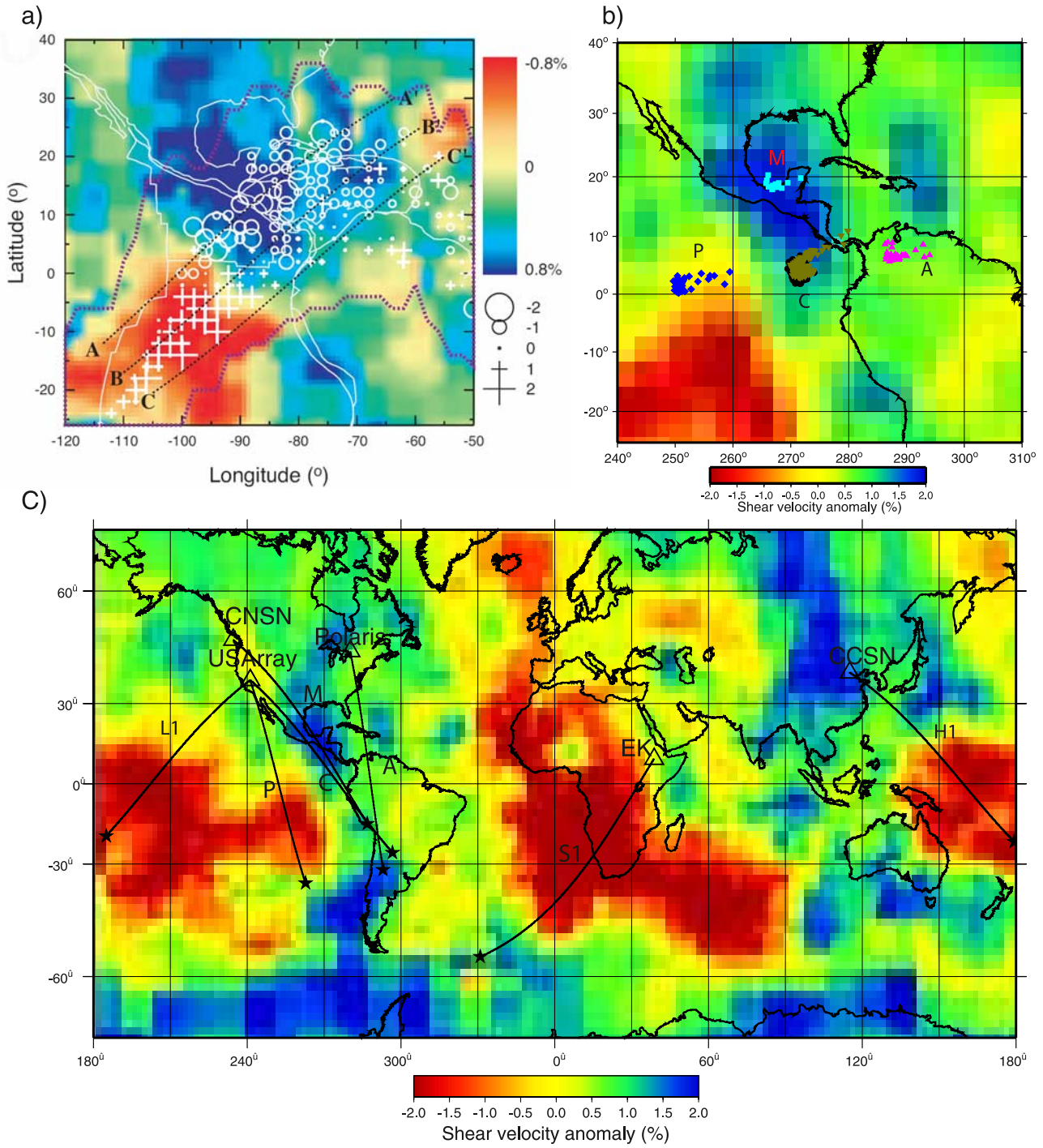

Figure 3. (a) Observations of (PKPab-PKPdf) residuals sampling beneath Central America along with proposed D″ *P* wave model in the background [*Sun et al.*, 2007b]. (b) A detailed map of Grand's tomographic image of Central America. The four subregions, P, A, C, and M are studied in detail where ScS bounce points are indicated in diamonds, triangles, inverted triangles, and squares, respectively. (c) Display of a map of events (stars) along with path geometry to various arrays (open triangles) superimposed on the tomographic results [*Grand*, 2002]. L1 [*Lay et al.*, 2006], H1 [*He et al.*, 2006], and S1 [*Sun et al.*, 2007b] paths were used to quantify the D″ structure beneath the slow-velocity regions.

zone comparisons of data with synthetics. To investigate the effects of different Clapeyron slopes on our phase boundary mapping, we tried four values of Clapeyron slope (γ = 3, 6, 9, 12 MPa/K). For each γ, we repeat the calibration process to find the $h_{ph}(\delta Vs)$, which matches the local triplication data in each zone. The h_{ph} becomes small when increasing γ for zone M and C. Both Zone M and C have relatively large positive velocity anomaly ($\delta Vs > 0$) and negative nonadia-

Table 1. Earthquake Used in This Study

Earthquake	Date	Time	Latitude (deg)	Longitude (deg)	Depth (km)	Related Subregion
1	10 Jul 2005	0446:31	−36.31	−97.26	10	P
2	13 Nov 2006	0126:34	−26.09	−63.34	557	C
3	26 Jul 2005	1411:36	−15.35	−72.96	110	M
4	17 Sep 2006	0934:09	−31.67	−67.00	105	A

batic temperature perturbation ($\Delta T < 0$). With negative ΔT in equation (2), the h_{ph} will decrease by increasing γ to make constant (h), which is required to fit the waveform data. If ΔT is a small perturbation, the contribution from ΔT in equation (2) is close to 0 and the change of h_{ph} is subtle for zone P and A. The same velocity jump $\beta(\delta Vs)$ are used for different values of γ to fit the amplitudes of the data.

[8] In each zone, β and h_{ph} are allowed to vary such that the predicted synthetic best matches the observed waveforms. We allow β to vary from 1.0 to 4.5% and h_{ph} from 50 to 300 km. Each combination is tested applying a grid search where the tomographic map (Figure 1a) is used as a reference model. The preferred combinations are given in Figure 4 where h_{ph} ranges from 100 to 240 km and β from 3.5 to 1.7%. The variable (δV_s) is defined relative to the tomographic model. The 1-D velocity-depth plot for the average ScS in each sample is given in Figure 4 (bottom) indicating the relatively large variation as a function of δV_S. The large low-velocity zone approaching the CMB is mostly an artifact forced by fitting the ScS-S predictions from Grand's model. However, adding a PPV to PV reduces this feature but is difficult to distinguish at these ranges [*Flores and Lay*, 2005; *Sun et al.*, 2006]. Thus, we concentrate on the upper PV to PPV phase transition.

2.1. Zone P

[9] As discussed earlier, there are very few samples of Scd beneath the Central Pacific because of the limitation imposed by the use of deep events and station source

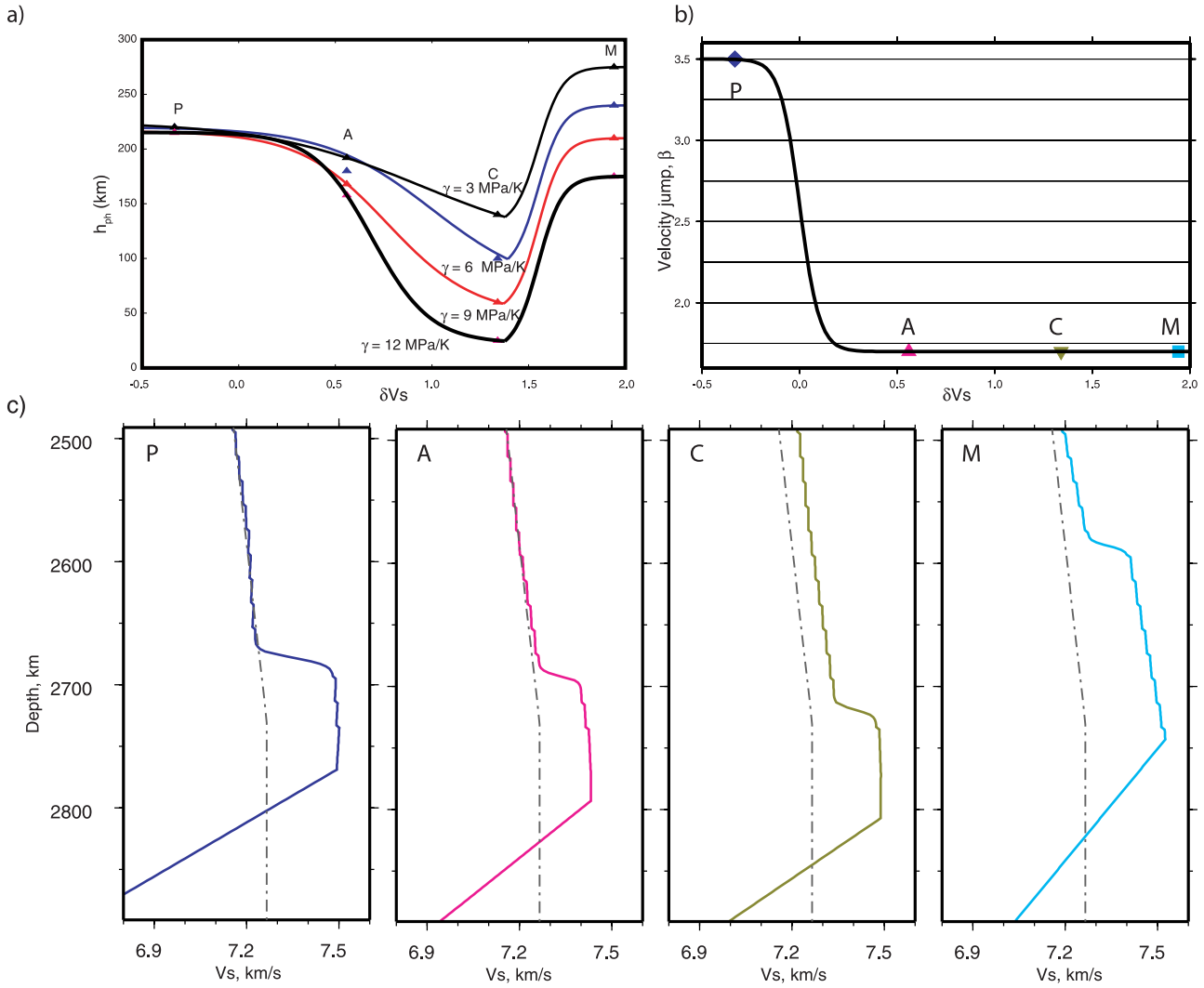

Figure 4. (a) Results from various subregions with $h(\delta Vs)$ for several values of γ and (b) $\beta(\delta Vs)$ which is the same for all values of γ. (c) Velocity profiles for the midpoint of each subregion is given along with PREM as a reference (dashed lines). Note that the raypaths for Scd are traveling horizontally at this point and are strongly influenced by neighboring structure as can be seen in Figure 3.

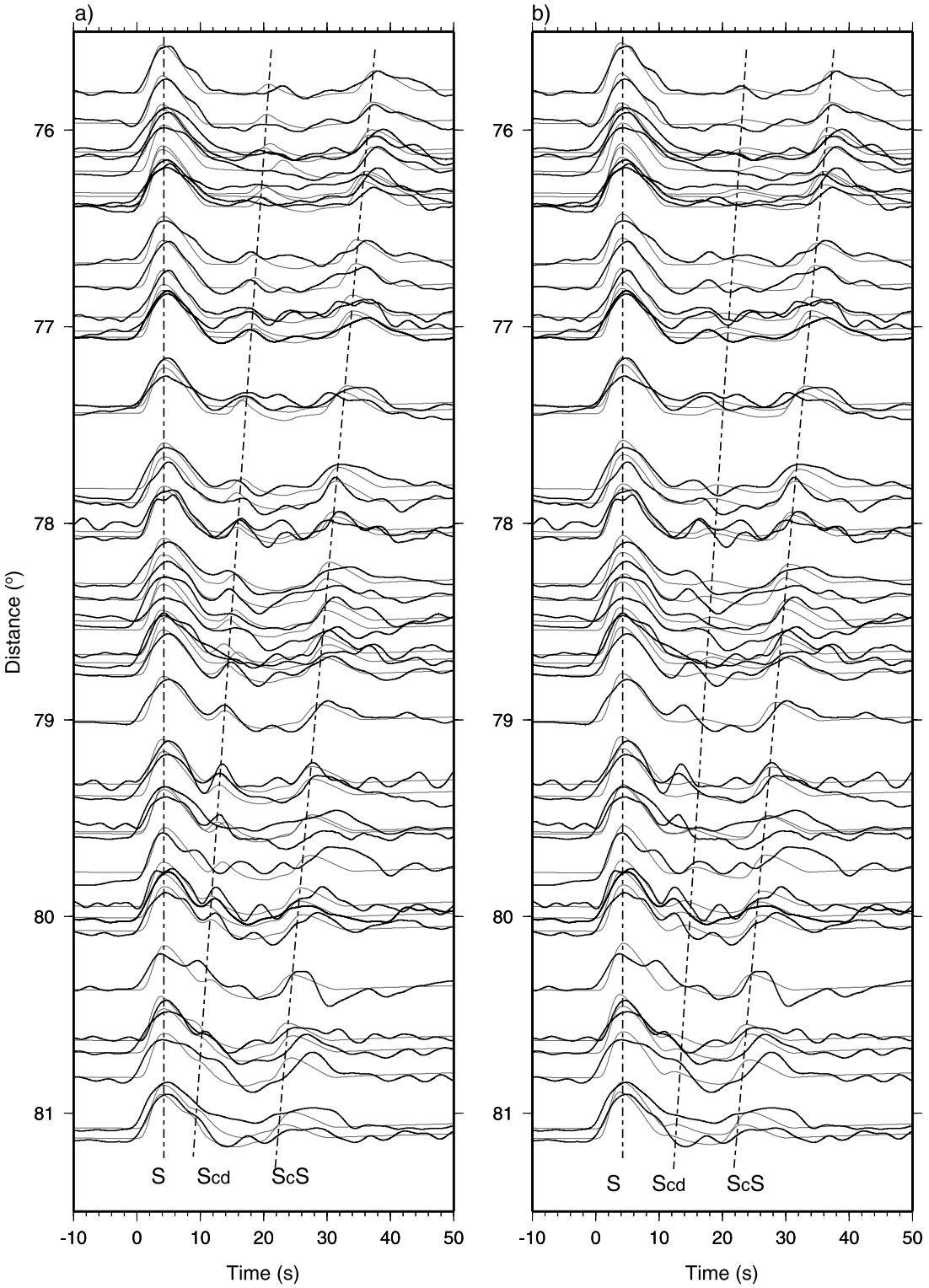

Figure 5. Display of synthetics (light traces) matching the recorded waveforms from area P (dark traces), which were recorded by the USArray of a shallow transform event (20050710). (a) The model has h_{ph} = 220 km and β = 3.5%. (b) Model has h_{ph} = 200 km and β = 1.5%. Dotted lines are added to indicate the three arrivals, *S*, Scd, and ScS.

geometry. However, it appears that USArray and other large arrays will allow sufficient data to identify Scd even from shallow events (Figure 5). This is a shallow transform event occurring on the Western Chile Rise (Figure 3c). We have plotted the data (SH component only) over the triplication distances expected. Since shallow strike-slip events generally produce two pulses of the same sign within a few seconds (*S* + sS), they merge together to produce one simple

pulse which is labeled *S* in the figure and idealized to the first synthetic pulse. There is some variation of the observed *S* pulse across the array which could be caused by shallow receiver structure [*Song and Helmberger*, 2007] or generated in the source region. However, both Scd and ScS appear to be recognizable. The tomographic model predicts the separation of (ScS-S) very well which can be expected from the detailed samplings of transform events by *Grand* [1994]. These 2-D synthetics were generated with the WKM routine [*Ni et al.*, 2000] along 2-D sections through the 3-D model. Note there are some variations along the record section caused by small changes in azimuth along the various paths. The reference height and velocity jump for this match is h_{ph} = 240 km, β = 3.5% where $\delta Vs = -0.5\%$ and assuming γ = 6 MPa/K. Synthetics generated by other γ models (Figure 4a) produce nearly the same results. Figure 5b contains predictions from the original *Sidorin et al.* [1999] mapping but with an updated tomographic map (S. Grand, personal communication, 2005), and where β = 1.7%. Obviously, the Scd is very small and late in these predicted synthetics.

[10] Because Scd is small relative to *S* and ScS in the data, it proves difficult to identify and measure accurately. At distances 76° to 78°, it is generally isolated but weak. At distance from 79° to 81°, it is generally stronger but can be contaminated by complex *S*. Even though our preferred model has about the correct timing on average, there are obvious rapid fluctuations in Scd observations both in strength and timing, i.e., near 76.2° and 78.6°. The synthetics show some of this scatter which appears to be associated with small changes in azimuth (Figure 3) as embedded in the tomography model. Allowing w_{ph} to vary could also affect such changes as indicated in Figure 6. Generally, Scd becomes smaller with increasing w_{ph} at these periods but variation in the tomography again causes fluctuations. Also, note that with w_{ph} = 25 km, the efficient transition occurs over 100 km (Figure 6b) because of the functional form in equation (1). This comparison of synthetics indicates that the w_{ph} parameter proves difficult to determine at this distance range. Thus for our purposes, we fix w_{ph} = 5 km. Much stronger effects are observed in the "C" samples as discussed later. The large β jump was required to generate a significant Scd pulse because the lower mantle velocity gradient is so low (Figure 4c) compared to fast regions [*Sidorin et al.*, 1998].

[11] The phase ScS is usually less well defined at this range where raypaths begin to sample the complexity of D." *Sun et al.* [2006] display attempts at modeling whole records by measuring a misfit coefficient based on cross-correlations (CC) both in displacement and velocity. Generally, simply overlying the observations with synthetics provides a very effective means of judging the goodness of fit. Here, we used this CC measure of fit but removed ScS by cutting the data and synthetics by 5 s before ScS. A plot of misfit errors for a grid search over β and h_{ph} is displayed in Figure 7 where we have included predictions from the *Sidorin et al.* [1999] model. By examining the record sections, one can easily pick out the better model. Although we have conducted such misfit calculations for all the data, we will simply display the best fitting synthetics in the following analysis assuming γ = 6 MPa/K.

2.2. Zone A

[12] The paths from these observations (Figure 8) sample a region nearest to PREM in that both *S* and *P* data (Figure 3) are relatively normal. The h_{ph} is about 175 km as displayed in Figure 4a when γ = 6 MPa/K. However, there is considerable variation in ScS–*S* times at ranges 77° to 78°. This feature is modeled quite well by Grand's tomographic model where the midmantle slab plays a strong role. We have plotted the comparison between data and synthetics in two ways, one aligned on *S* arrival (Figure 8a) and one aligned on predictions from the IASP91 reference model (Figure 8b), which displays obvious variation in *S* travel times. Note that now ScS plots more on a line as well as Scd. Features such as this are becoming more recognized with the advance of more arrays and makes the Scd mapping even more challenging.

2.3. Zone M

[13] This sample (Figure 9) was obtained mostly from the Canadian National Seismic Network, Figure 3c. It contains the fastest D″ velocity regions comparable to those found beneath Central Asia [e.g., *Wysession et al.*, 1998]. The tomographic results do not predict the sScS-sS differential times as well as other samples suggesting that the D″ structure needs to be faster. However, the Scd phase is quite clear and easily modeled yielding an h_{ph} = 240 km. The direct *S* phase was weak (nodal) which is why we have displayed the sS profile of data. The depth effect helps to separate (sScd – sS) and aids in identifying and characterizing the strength of Scd. We have calculated synthetics with parameters from the zone "C" (Figure 4) to emphasize the difference in Scd ampling. Although not displayed, predictions from the *Sidorin et al.* [1999] model does quite well for this section since he assumed a similar β = 1.5%. Thus, our new model will predict results quite similar to his in fast regions.

2.4. Zone C

[14] This sample is in a region where many detailed studies have been conducted, where rapid changes have been reported indicating some strong and some very weak Scd observations [*Garnero and Lay*, 2003]. Migration of the array data suggests complex features with interbedded layers of velocities [*Thomas et al.*, 2004]. Some of this variation can be seen in our sample C as recorded by USArray but reasonably modeled with h_{ph} = 100 km as displayed in Figures 10a and 10b for ranges less than about 78.5°. We have included two sensitivity displays indicating the effects of changing β = 3.5% (Figure 10c) and assuming β = 1.7% (Figure 10d) but changing the h_{ph} to that used in zone *P* (220 km). These two results do not fit the data as well and indicate relatively delayed Scd relative to *S* which is distinctly different than that predicted by the Sidorin's model as discussed in the next section. Beyond about 78°, the Scd raypaths sample the edge of the fast blue zone as displayed in Figure 3b and greatly complicate the waveforms. Some of this complexity is addressed by *Sun et al.* [2006] and *Helmberger et al.* [2005], where both WKM and finite difference modeling was discussed. This laterally varying D″ region is also discussed by *Thorne et al.* [2007] where some 2-D structures suggest double Scd arrivals. We will address some of these issues in the next

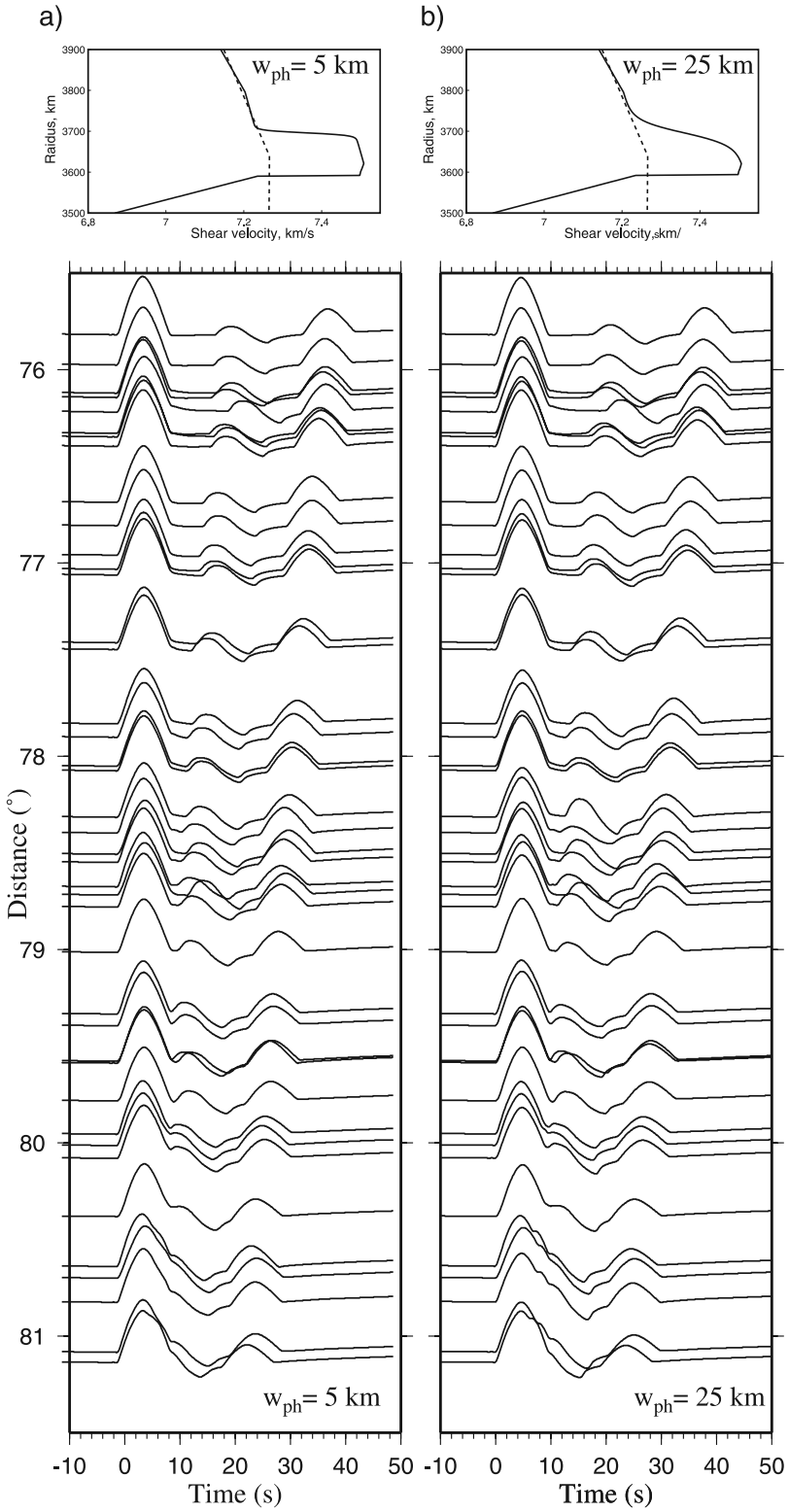

Figure 6. Comparison of a sensitivity test involving changes in w_{ph} from (a) 5 km to (b) 25 km. The synthetics are calculated for zone P with h_{ph} = 220 km and β = 3.5%. The top panel shows the 1-D vertical profiles (solid lines) in the middle of zone P for different w_{ph} along with PREM model (dash lines).

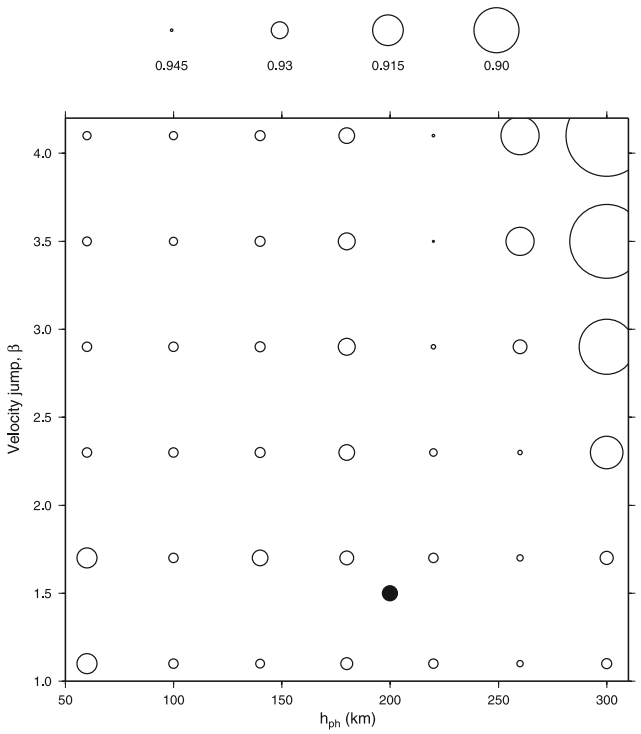

Figure 7. Display of misfit errors in modeling the data for area P where the preferred parameter search yields $\beta = 3.5\%$ with $h_{ph} = 220$ km. The black dot is the solution predicted by Figure 1b using the mapping proposed by *Sidorin et al.* [1999]. The circles denote the error measure defined by (1-CC), where CC is the cross-correlation coefficient over the *S* and Scd wave train. The smaller circle means the larger value of CC.

section by including these very late Scd arrivals which are sampling the edge of the fast blue zone.

3. Mapping, Predicting, and Refining

[15] In this section, we will apply the parameters determined in the previous section in generating a new hybrid model. The model is still based on Grand's tomographic images and the relationship given in equation (2). However, uniform h_{ph} is now replaced by $h_{ph}(\delta V_s)$. We assume that the bottom 240 km of Grand's model or D″ can be used to estimate regional differences. Grand's present model is presented in $2^\circ \times 2^\circ$ grids and contains a small velocity jump at 240 km above the CMB in the reference 1-D model. This feature is smoothed out and a large number of layers and elements applied as in the work of *Sidorin et al.* [1999]. We then average the velocity perturbations in a circular cylinder over the depth of 240 km with a radius of 2° to establish δVs. This δVs is then used to fix h_{ph} assuming the curve in Figure 4a. The map of the phase height in Figure 11a is constructed in this manner assuming $\gamma = 6$ MPa/K. Note that even though the slowest and fastest regions have about the same h_{ph} their actual phase height is strongly modified by the tomographic model (roughly 50 km to 300 km) because of the temperature effect implied by the tomographic model. The 3-D velocity model is then generated by adding the variation in β in equation (1) as modified to agree regionally with Figure 4b. Cross sections along a radial cut (AA′) and along constant azimuth (BB′) are displayed in Figures 11b and 11c. The yellow halo-like structure in Figure 11a appearing around the raised plateau is caused by point C in Figure 4a and predicts the strong drop in elevation at the edges of the original supposed buckled slab. Raypaths along two azimuths, one sampling the edge along the yellow trough (CC′, Figure 11d) and one sampling the fast blue zone essentially along section DD′ (Figure 11e) have been included in 2-D tomographic images. Obviously, we expect to see considerable complexity bracketed between these two azimuths, especially along CC′. We have included some example raypaths displaying the structure sampled by USArray in Figures 11d and 11e. The sampling of the phase boundary (Scd) becomes very complex.

[16] Figure 12 displays some of these features where the ScS bounce points are indicated for two "fan shots" with one crossing the blue structure (red arc) and one just south of the structure in black. We generated 2-D synthetics (Figure 12b) at a constant distance of 79.5° for event A assuming two depths (150 km and 600 km). These synthetics are aligned on PREM prediction. Note that Scd is particularly late at azimuths less than 280° and shifts rapidly forward near 290° and again between 315° and 330°. The Scd timing changes by over 12 s and its amplitude changes by about a factor of 3 along with significant wave shape distortions caused by in-plane multipathing. Near 320°, the Scd phase shifts quite close to *S* for the deep event which could easily be enclosed within the *S* phase, thus making it disappear abruptly.

[17] These synthetics become even more complicated when we include azimuthal multipathing as displayed in Figure 12c. To emphasize the variable nature of the 3-D synthetics, we have plotted each trace aligned relative to PREM prediction. Thus, paths with azimuth greater than about 335° sample the fast velocities beneath the Midwest and eastern seaboard producing earlier arrivals than PREM prediction while those to the west are about 6 s late. This difference in travel times is caused by the rapid change in upper mantle structure when crossing the Rocky Mountain Front and is well known [*Helmberger et al.*, 1985].

[18] The 3-D synthetics (Figure 12c) were generated from neighboring 2-D sections sampling the Fresnel zone by applying diffraction operators [*Helmberger and Ni*, 2005a]. Rapid travel time changes near the fastest geometric ray can cause the pulses to spread out (multipath), i.e., near 275° or spike up as at 340°. These features are essentially controlled by the travel time curvature as a function of azimuth. It can affect all phases but appears to be particularly strong for Scd. This feature could be the reason for the apparent unstable nature of Scd detection [*Garnero and Lay*, 2003]. Both the 2-D and 3-D synthetics show a jump near 320° for ranges near 81°. This feature is more subdued in the 79° fan section since the fast structure is slightly removed from the boundary (black arc in Figure 12a). Some of the predicted changes can be tested against existing data with some success as displayed in Figure 12d. The data contains paths to California (in black) and to Colorado (in red). Note that Scd is stronger and delayed in the California stations at ranges greater than 80.5° and nearly the same at shorter distance. The synthetics in Figure 12c display a

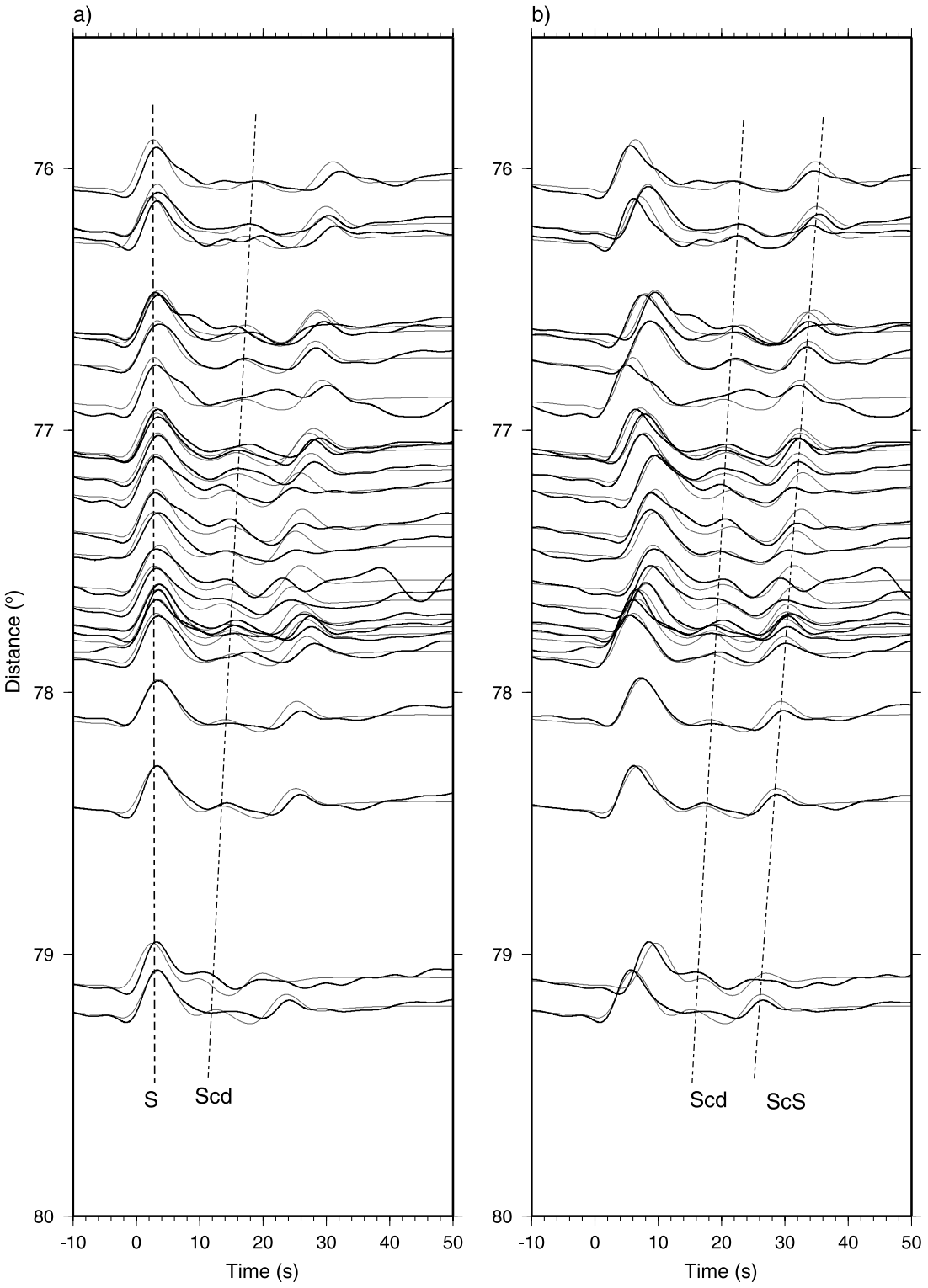

Figure 8. Display of best fitting synthetics (light traces) for record sections sampling area A recorded by the POLARIS array of a deep South American event (20060917). The model has h_{ph} = 180 km and β = 1.7%. The displacement profiles are aligned (a) on the arrival of *S* and (b) on the predicted arrival of *S* for the IASP91 model. Note the remarkable predictions of *S* arrival times form the tomographic model.

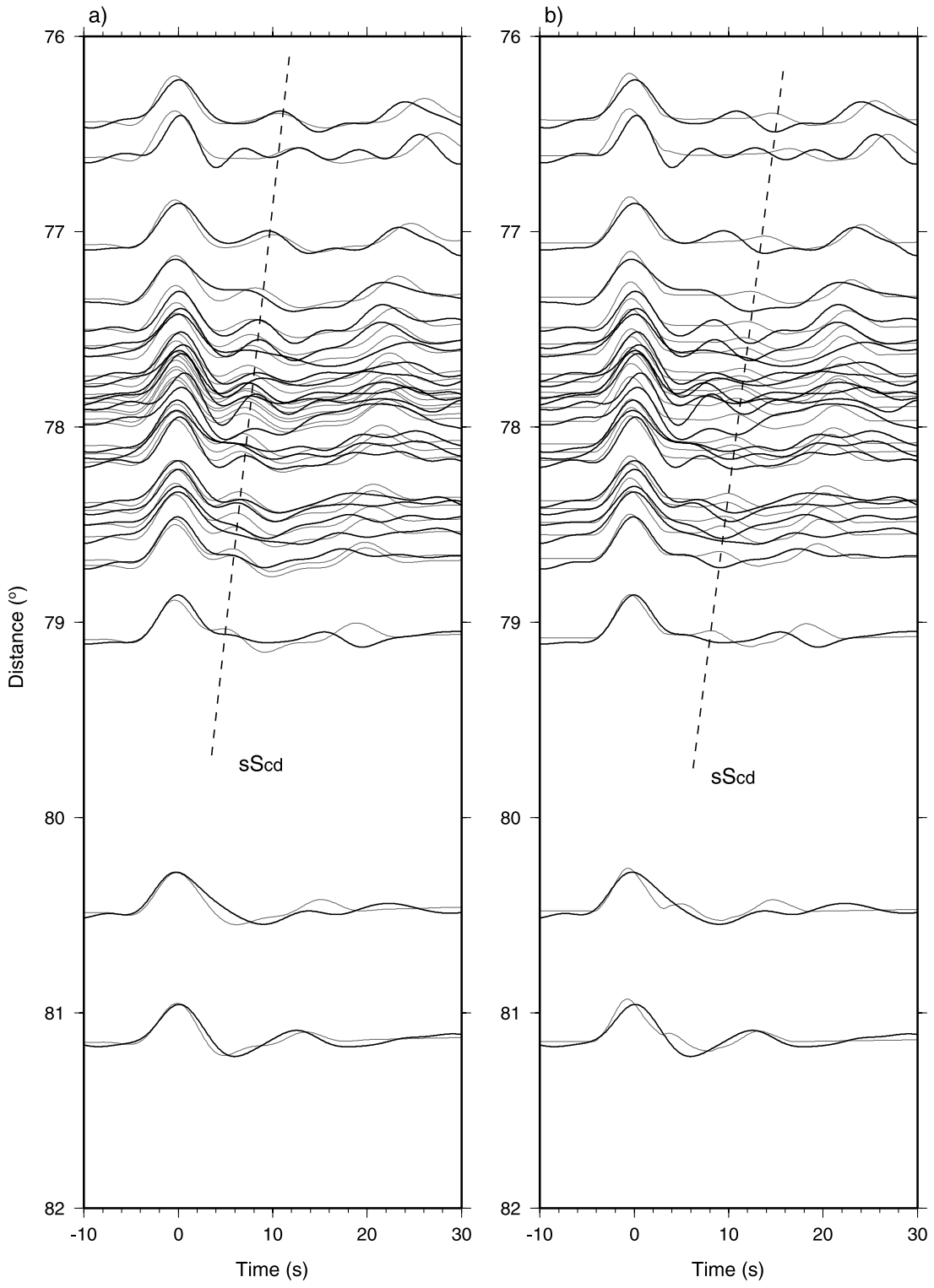

Figure 9. Comparison of synthetics (light traces) with observations (dark traces) from the western Canadian stations of a South American event (20050726). (a) For model, h_{ph} = 240 km and β = 1.7%. (b) The synthetics are produced by a model with h_{ph} = 100 km and β = 1.7% to indicates sensitivity relative to the model for zone C.

similar pattern as outlined in red and black zones. However, the differences predicted by the model are not severe enough which requires some added refinement by lowering the trough along the fast region or adding a ULVZ at the CMB. This zone at the edge of the blue structure will be well-sampled by USArray as it develops and the details of this interesting structure can be improved. A sample is displayed in Figure 13a. Note the abrupt change in character

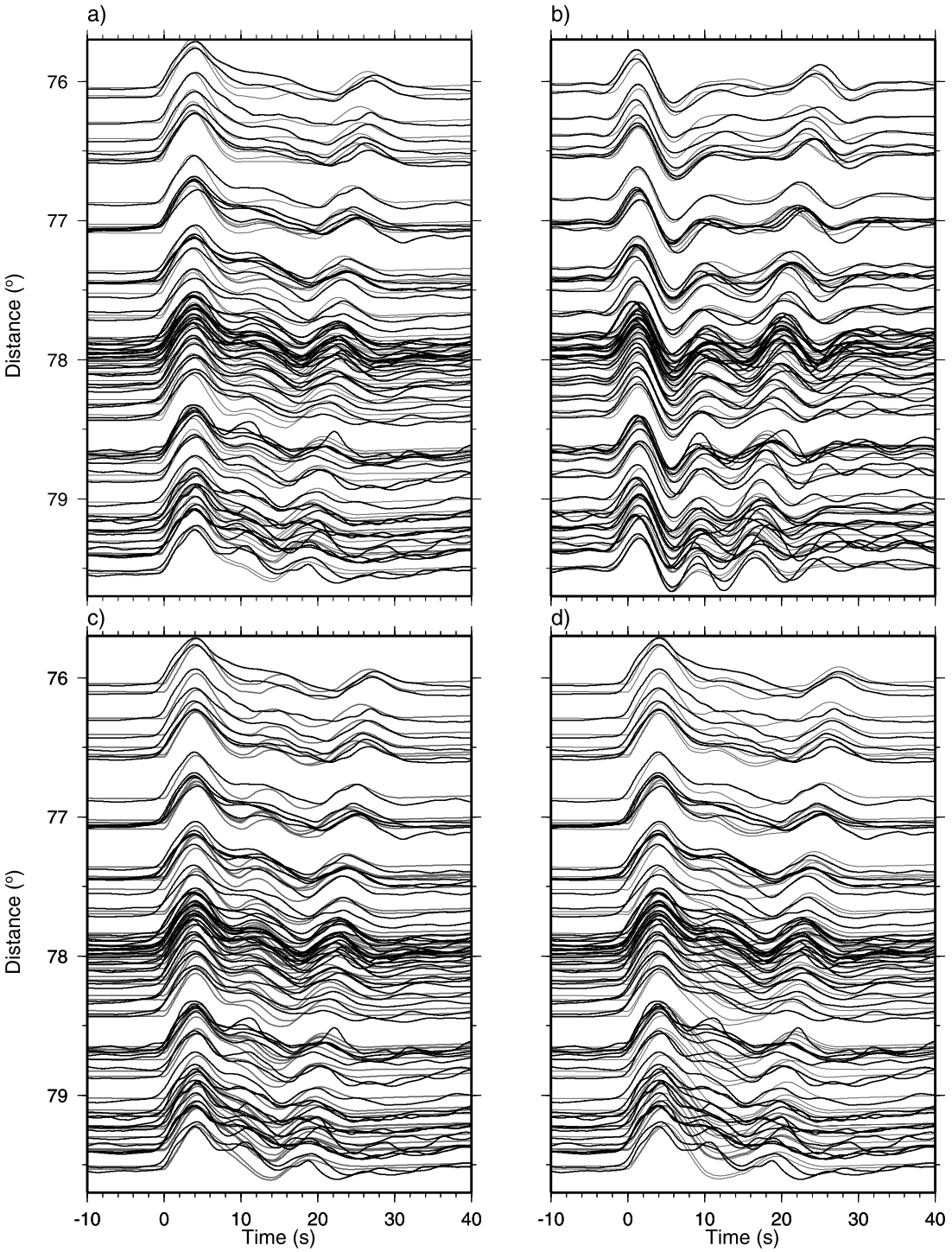

Figure 10. Comparison of synthetics (light traces) and observations (dark traces) sampling subregion C of a deep South American event (20061113). (a) The displacement profiles for a model with h_{ph} = 100 km and β = 1.7%. (b) The velocity profiles for the same model. (c) A model defined by h_{ph} = 100 km and β = 3.5% and (d) a model with h_{ph} = 220 km and β = 1.7%. Note that fits in Figure 10b are relatively good at distances less than 78.5°.

in the gray zones where the raypaths encounter the sharp jump in phase height. Beyond this range, the Scd becomes difficult to identify and the ScS phase become complicated. The ScS phase should become asymptotic to *S* in travel time at the larger ranges assuming a PREM model; however, ScS becomes weak and delayed for many samples. The synthetic predictions are given in Figure 13b and display a similar disruption but shifted slightly to shorter distances. Shifts of this magnitude are common when attempting to model differential phases assuming enhanced tomographic images [*Helmberger and Ni*, 2005b].

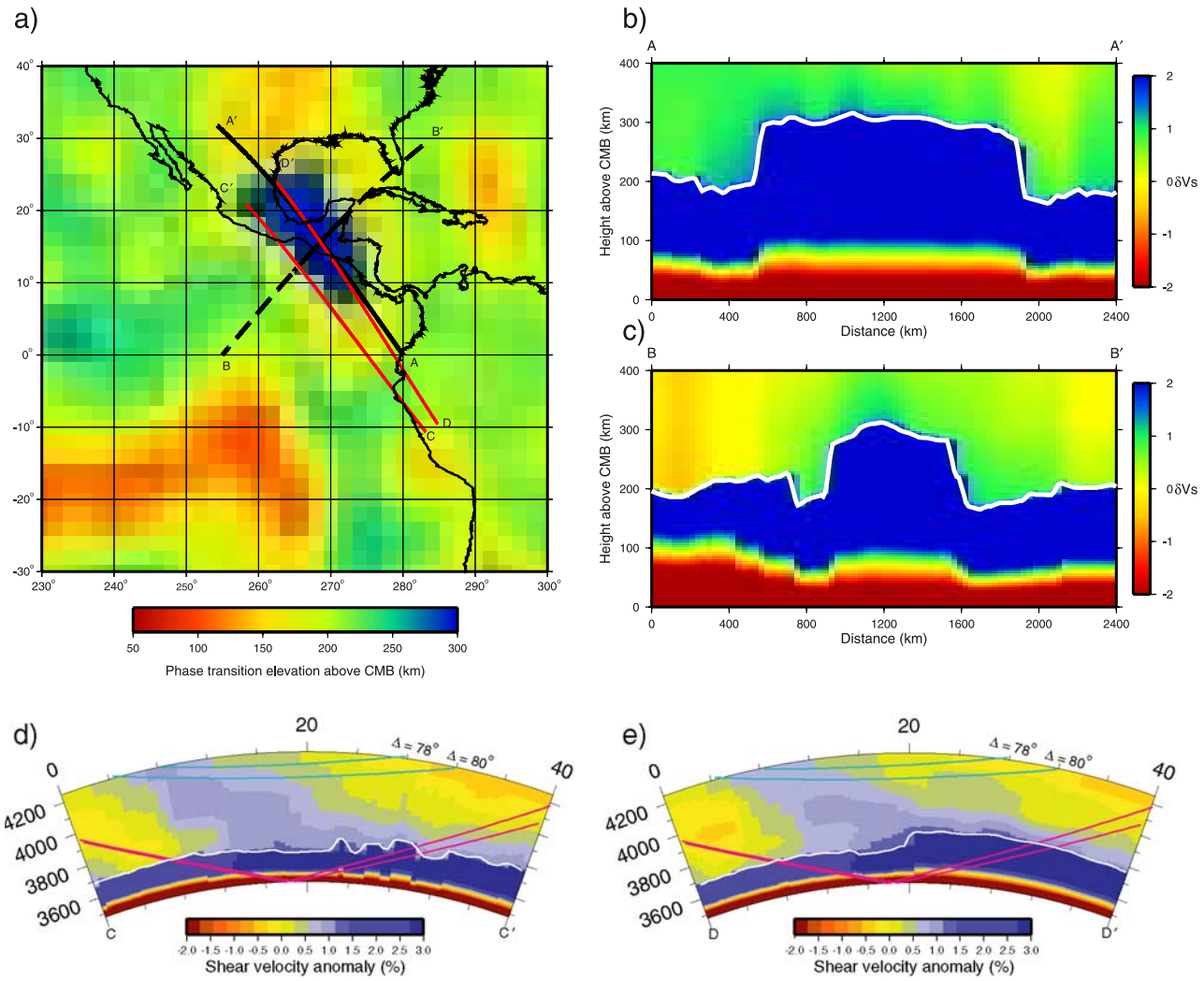

Figure 11. Detailed display of phase boundary topography; the phase boundary variation beneath Central America. Velocity cross sections along profiles (b) AA′ and (c) BB′ sampling the raised structure. The phase boundary is indicated as white lines. The cross section along path (d) CC′ and (e) DD′ from an event in South America. Raypaths are included for *S* (blue) and ScS (red).

[19] We present (ScS-S) predictions from our model in Figure 14a where we have included a large number of data samples measured from the recent USArray data. The white symbols are differential times from the (ScS-S) waveforms presented earlier in Figure 13a. The differential values are small and slightly negative at ranges 75° to about 84° and positive thereafter. Some large delays occur beyond 85°. Note that these values occur for bounce points slightly under the elevated phase boundary as displayed in Figure 14b. These large delays can be explained by adding a ULVZ layer (20 km thick with a shear velocity drop of 30%). However, most of the delays fall along the model predictions. The other symbols are from events along the same corridor but tend to be negative indicating that ScS is early, probably caused by the high-velocity PPV layer.

[20] Several researchers have reported on ULVZs near about N7.5°W90°, i.e., *Revenaugh and Meyer* [1997], and more recently *Sun et al.* [2007a]. The latter study uses the cross-correlation of PKPab to PKPdf to detect rapid changes in velocity with scale lengths similar to those in Figure 14b. Low values of cross-correlations have been modeled by *Luo et al.* [2001] with small pockets of ULVZs. It appears that another line of ULVZs exists along the eastern boundary of the elevated phase boundary although we await USArray for a detailed ScS-*S* sample of this edge. Last, note that the large offset in Scd travel times reported by *Hutko et al.* [2006] occurs along the southwest corner of our structure in good agreement with their observation.

4. Discussion and Conclusion

[21] In this report, we have revisited the earlier phase transition mapping generated by *Sidorin et al.* [1999, Figure 1b]. Their paper used the relative timing between Scd and *S* to determine γ = 6 MPa/K, β = 1.5% (velocity jump), and global phase boundary reference height h_{ph} = 200 km. This model predicts relatively uniform and strong Scd beneath fast regions but very small signals in other

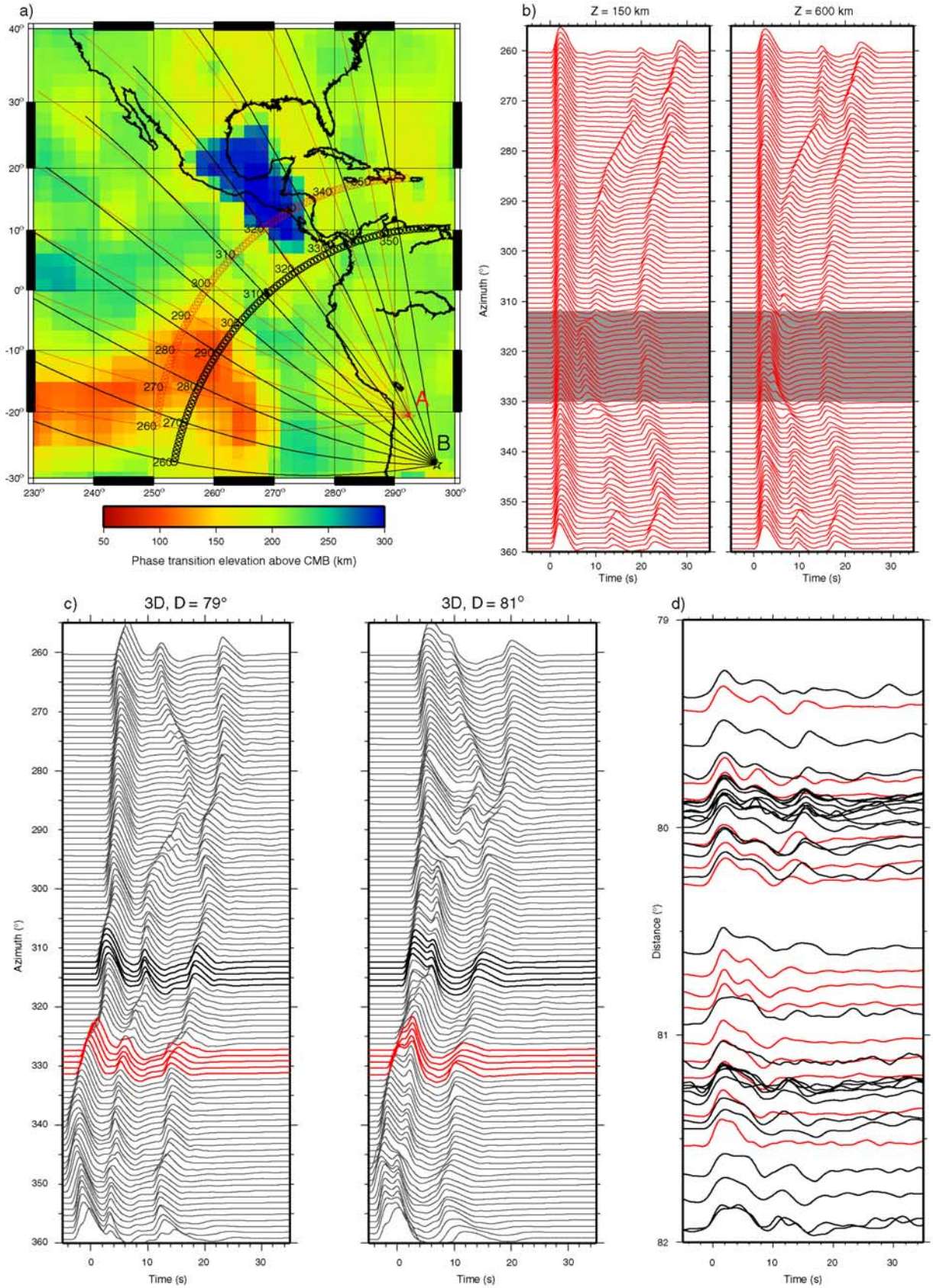
a)
b)
Z = 150 km
Z = 600 km
Azimuth (°)
Time (s)
A
B
Phase transition elevation above CMB (km)
c)
3D, D = 79°
3D, D = 81°
d)
Distance (°)

Figure 12

regions [*Kendall and Shearer*, 1994; *Russell et al.*, 1998]. Recently, broadband array measurements have demonstrated relatively strong Scd in regions other than the Pacific Ring of high velocities [*He et al.*, 2006; *Lay et al.*, 2006; *Sun et al.*, 2007b]. We have solved this mapping difficulty by using waveform information and matching synthetics against observations for four well-sampled regions. The most significant difference between our results and the earlier model is the added strength of Scd in slow regions and the sharp gradients (Halo-like structures) around the fastest zones. A comparison of the two models is given in Figure 14c along with recent results from *Wang et al.* [2006] and *van der Hilst et al.* [2007] using a new inverse scattering method. These profiles essentially cross the structure along the same section with the fastest shear wave anomaly beneath the middle portion. In Figure 14c, note that the left end of L1 ends at the same position where the new model steps down and there is a short span of weak signals in the upper images before stepping back up. Their images also show an enhancement in low velocities just above the CMB beneath the elevated jump.

[22] While the sharp contours in the phase boundary are becoming clearer in the *S* velocities, the *P* velocities appear to vary smoothly across this region (Figure 3a). This feature can be explained by the lack of any significant Pcd observed for this region [*Ding and Helmberger*, 1997] and the predictions from mineral physics [*Hirose*, 2006]. In short, the phase boundary structure appears to be a shear velocity feature where the high-velocity slab material produces smooth high velocities in both *P* and *S* but no sharp feature without the phase change. While the smaller-scale ULVZ-type features are interesting, we still lack a detailed description of where they are and their relationship with our model. However, small-scale features of this description are predicted by some dynamic models [*Tan et al.*, 2002]. They also predict small-scale plumes along these boundaries which could help explain the sharpness of the mapped structure (Figure 14c). Upwelling could cancel the cooling influence of the slab debris and, perhaps, the phase change sharpness as well. This transition from fast-to-normal velocities is probably not that well imaged by tomography and awaits high-resolution studies.

[23] Last, one could speculate on the role of temperature gradient, δT, in controlling the phase transition. Note that we have assumed a sharp phase transition (w_{ph} = 5 km) in the above analysis. Perhaps, the phase transition has a more uniform onset globally but variable sharpness where the bulk of the transformation from PV to PPV takes place as mentioned earlier in Figure 2 and Figure 6. *Ohta et al.* [2008] demonstrated that postperovskite phase transition in both pyrolitic and MORB materials occurs within a 5 GPa pressure range, which correspond to a lower mantle depth range of 90 km. The seismic synthetics for models with different transition thicknesses (Figure 6) indicate that seismic data are not particularly sensitive to the sharpness of the phase transition at the distance ranges of 75°∼85°.

[24] Another difference between the new model and Sidorin's old model is the shear velocity jump for slow velocity regions. The 3.5% velocity jump across the phase boundary is much higher than Sidorin's velocity jump (1.5%) and theoretical calculation for perovskite to post-perovskite transition (−1%−1.5%) [*Ohta et al.*, 2008]. If a high degree preferred orientation of postperovskite is needed to explain this high shear velocity jump, a strong anisotropy is expected in the lower mantle in this region [*Hirose*, 2006].

[25] Significant seismic anisotropy has been observed in several regions the lowermost mantle [*Matzel et al.*, 1996; *Garnero and Lay*, 1997; *Lay et al.*, 1998; *Thomas et al.*, 2007]. Beneath the D″ discontinuity, the detected horizontally polarized *S* wave velocity (V_{SH}) is faster by 1−3% than the vertically polarized *S* wave velocity (V_{SV}). *Sun et al.* [2007b] report the existence of the D″ discontinuity beneath the center of African Superplume (slow velocity region) from the SV component. The different anisotropy behaviors between the fast and slow velocity region could be related to the dynamic flow pattern in each region. At the edge of the fast velocity region, the flow pattern could be greatly affected by the buckled slab, which will produce complicated Scd behavior in such regions.

[26] With the function of $h_{ph}(\delta Vs)$ and $\beta(\delta Vs)$ defined as in Figure 4, we can generate global phase boundary maps (Figure 15) for various γ assuming Grand's tomographic model. Small values of γ produce smooth variations of the phase boundary. When γ = 3 MPa/K, the heights of the phase boundary above CMB (h) beneath Africa and Central Pacific (slow velocity region) are larger than 150 km. The phase boundary height beneath Central America and Eurasian (high-velocity region) is about 300 km. For increased γ, the difference of h between the slow velocity and high velocity region becomes larger. The height of phase boundary is ∼50 km beneath Africa for γ = 9 MPa/K. *Sun et al.* [2007b] obtained evidence for a possible phase change at about 80 km above the CMB beneath South Africa which is in rough agreement. Although it is difficult to sample the D″

Figure 12. Simulations of seismic sections sampling the complex geometry of the phase boundary variation. (a) The phase boundary variation beneath Central America. The red circles are ScS bounce points on the CMB for a "fan shot" for an event A in South America (red star) at distance of 79.5°. The black circles indicate ScS bounce points for a "fan" shot for event B at a distance of 79° assuming a source depth of 600 km. (b) The 2-D synthetics generated for event A at two different depths, 150 km and 600 km. The shaded zone indicates the sampling of the region of high phase boundary elevation (blue zone in Figure 12a). Records are aligned on the *S* phase. (c) The 3-D synthetics for event B at distance 79° and 81°, which align on IASP91 travel time predictions. The dark black traces correspond to azimuths toward California (TriNet) and red traces relative to Colorado Stations (CDROM). (d) Record sections for an event (20000423) with the same location of event B in Figure 12a. The black traces are recorded by TRInet which are at smaller azimuth and relate to the dark black traces in Figure 12c. The red traces were recorded by CDROM array at large azimuth and relate to the red traces in Figure 12c.

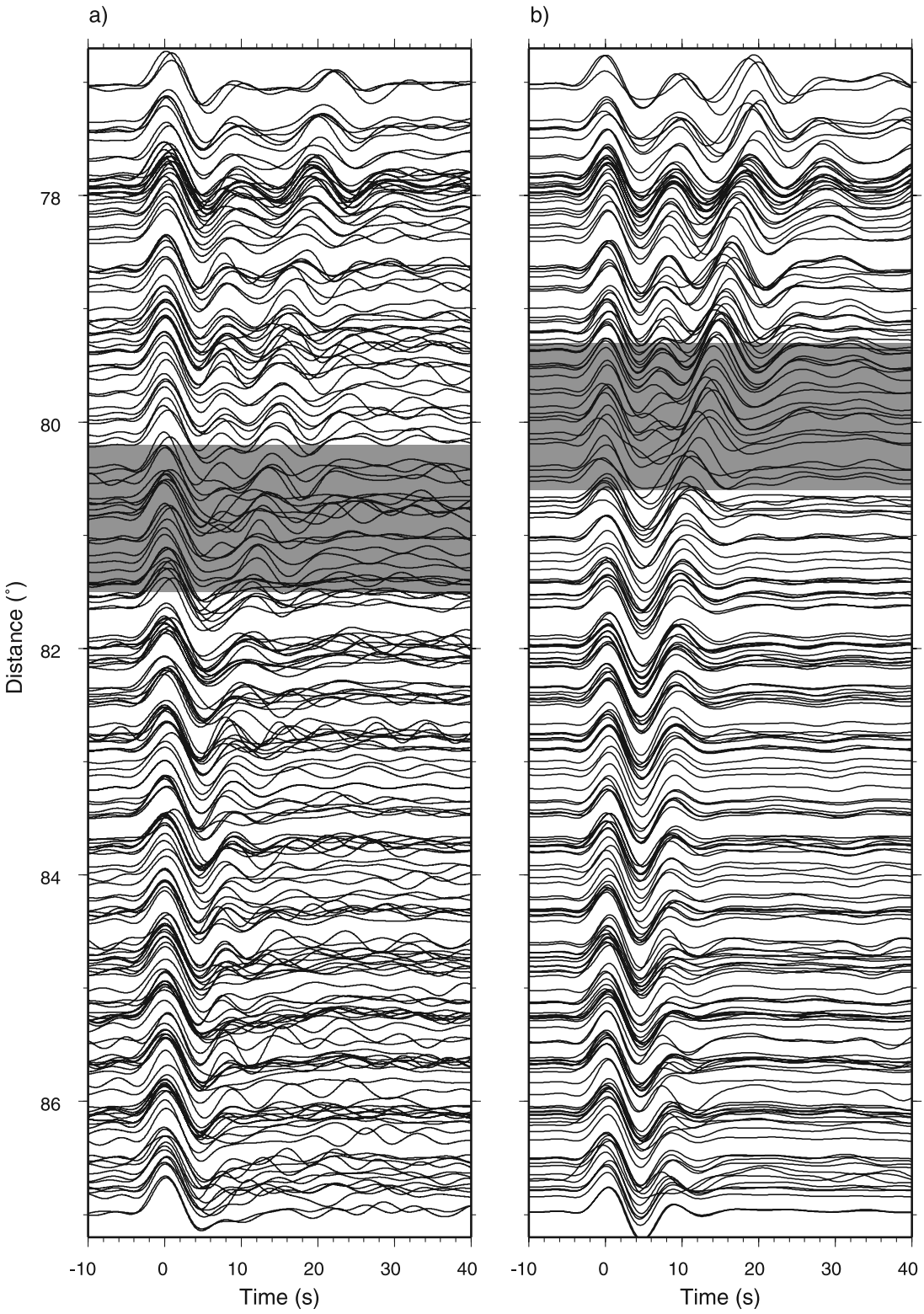

Figure 13. Comparison between (a) data and (b) synthetics in velocity for event 20061113. The regions with rapid variation of Scd are marked with shaded area.

region beneath the slow regions because of source-receiver locations, these few observations suggest that $\gamma > 6$ MPa/K.

[27] On the basis of the above analysis, we can estimate the global mantle temperature at the phase boundary. We assume a reference point with the pressure (P) of 124 GPa and the temperature (T) of 2500 K [*van der Hilst et al.*, 2007]. All the phase boundary lines with different γ intersect at this reference point. The temperature for given

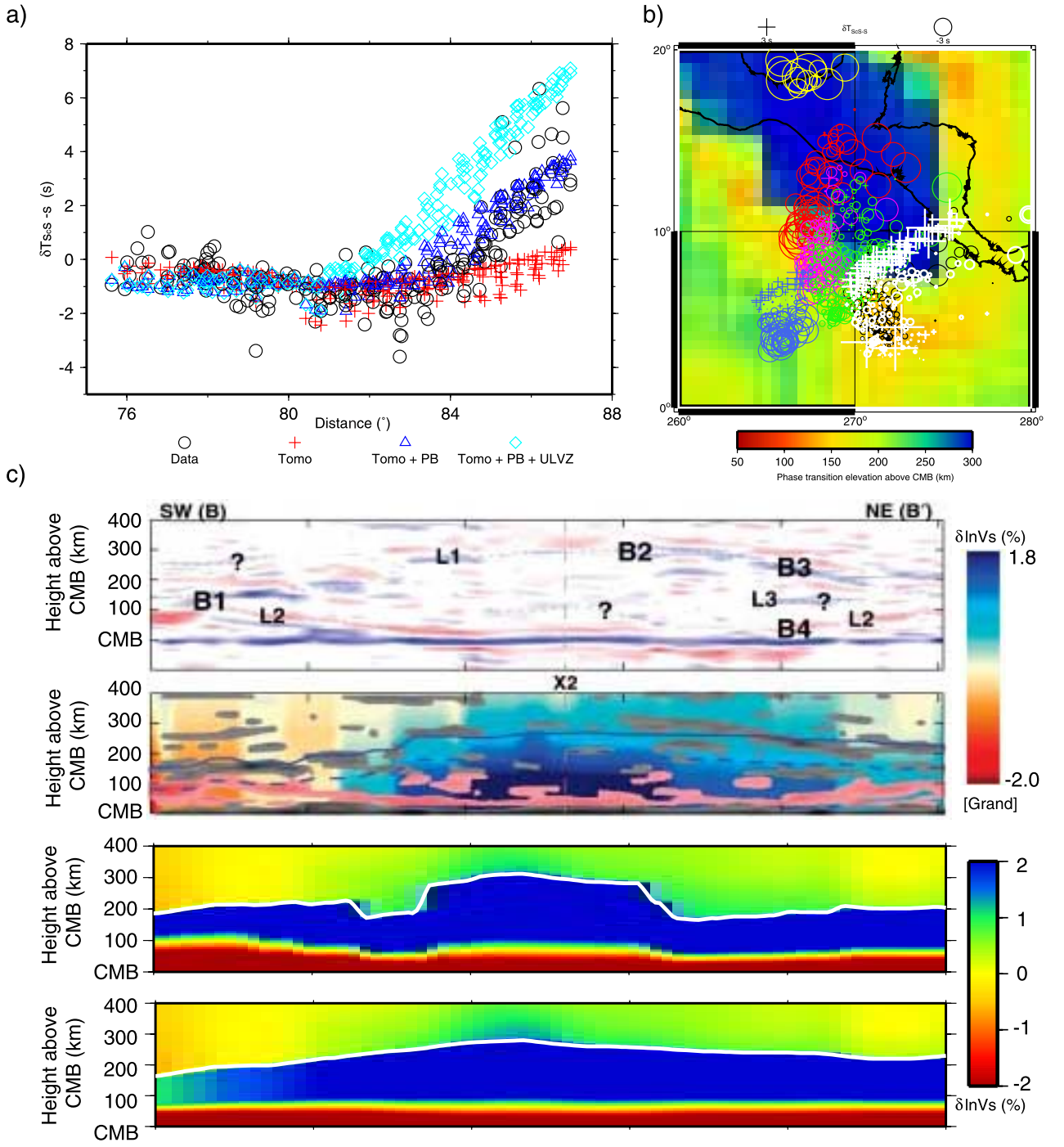

Figure 14. (a) The data (event 20061113 in Figure 13) and the predictions for the differential ScS-S residuals. The models are Tomo (Grand's tomography model), Tomo+PB (phase mapping model), Tomo+PB+ULVZ (phase mapping model adding a ULVZ layer with 20 km height and −30% shear velocity reduction at the base of the mantle). (b) The observed residuals of the differential ScS-S travel times with respect to PREM are plotted at the bounce points of the ScS on the CMB. Positive and negative residuals are indicated by the crosses and circles. Different colors relate to different events beneath South America. The bounce points of event 20061113 are marked by white symbols. (c) A comparison of results from different methods of phase boundary imaging. The upper two models in Figure 14c display reflectors from inverse scattering techniques with positive reflections in blue (dark gray) and negative in pink [after *van der Hilst et al.*, 2007]. The lower of these two show enhancement of the reflecting along with a solid blue line indicating phase transition location from the original Sidorin et al.'s model superimposed on Grand's tomography profile [*Grand*, 2002]. The bottom two models in Figure 14c are our new phase boundary model and Sidorin's model [*Sidorin et al.*, 1999]. The phase boundary is indicated by white lines.

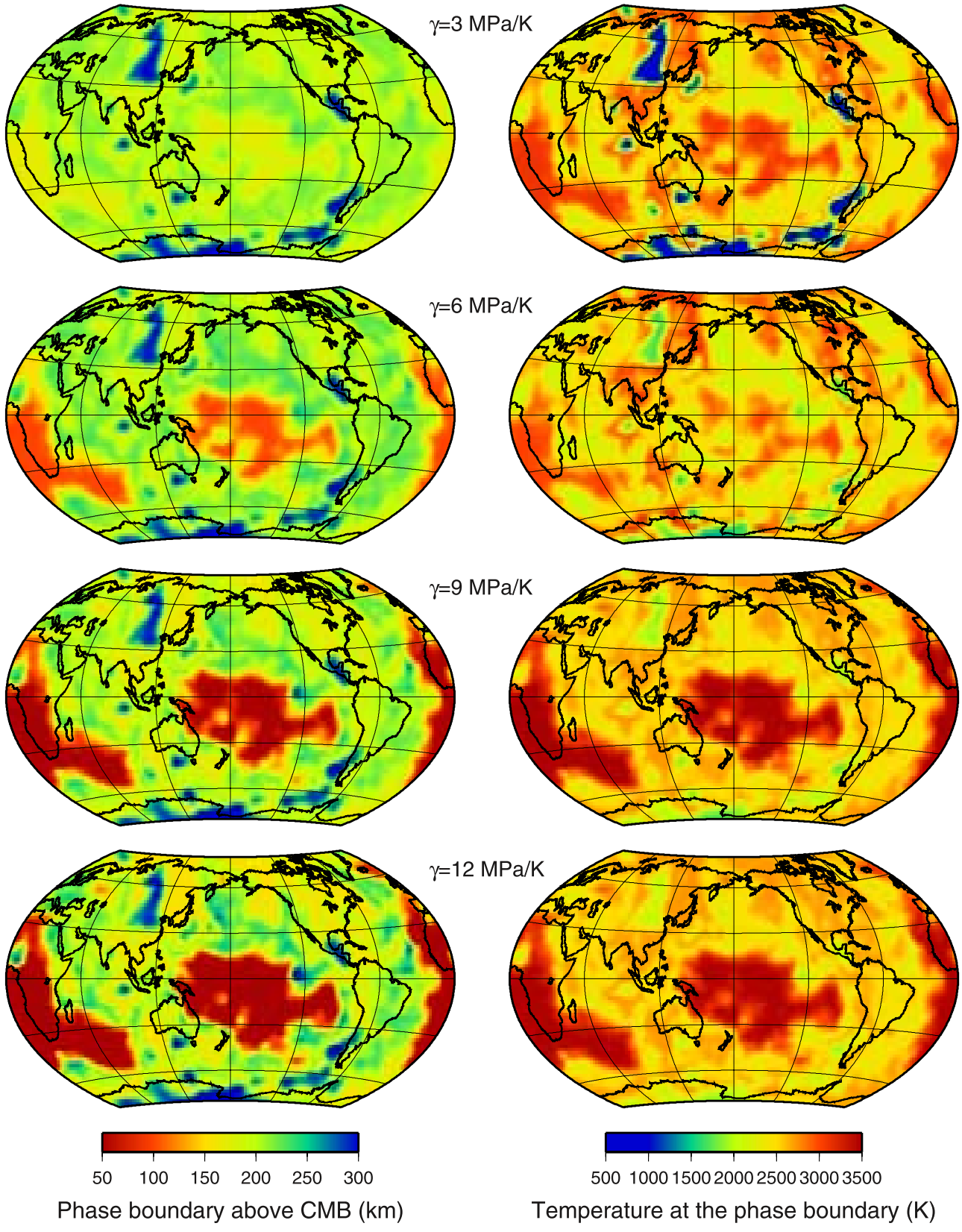

Figure 15. The global prediction of (left) phase boundary height above CMB for various values of γ and (right) temperature at the phase boundary for these γ.

height of the phase boundary can then be estimated by assuming

$$T = 2500 + \frac{P - 124}{\gamma}. \quad (3)$$

The global temperature distribution at the phase boundary is shown in Figure 15. When $\gamma = 3$ MPa/K, the temperature at the high velocity region is less then 600 K. The high velocity region is believed to be related to an old subducted slab, which has much higher temperature than 600 K [*Tan et al.*, 2002]. Therefore, values of γ larger than 6 MPa/K are required for producing reasonable temperature for the slab debris in the lowermost mantle based on present PV-PPV experiment results. A large γ ($\gamma \approx 9$ MPa/K) agrees with the results on reconciling the core temperature and postperovskite double crossing [*Hernlund and Labrosse*, 2007] and recently experimental result with the MgO standard [*Hirose*, 2006].

[28] The chemical heterogeneity in the lower mantle has been well accepted. Unavoidably, the change of chemistry will add more complexity to the phase boundary [*Ohta et al.*, 2008]. Moreover, the local dynamics will play an important role on the phase change. For example, the edge of a subducted slab just above the CMB could trap significant heat [*Tan et al.*, 2002], which will move the phase boundary toward the CMB (Zone C). To address these questions will require further efforts in geodynamics, mineral physics, and more detailed seismological studies.

[29] **Acknowledgments.** We would like to thank two reviewers and the Associate Editor. Their suggestions and comments were greatly appreciated and made significant improvements to the manuscript. We also thank discussion with Mike Gurnis and Eh Tan. Data were provided by IRIS data centers, Canadian National Seismograph Network, and POLARIS Network. All maps in this paper were produced using GMT developed by Paul Wessel and Walter H. F. Smith. This work was supported by National Science Foundation grants EAR-0456433 and 0639507. Contribution number 10005 of the Division of Geological and Planetary Sciences, California Institute of Technology.

References

Anderson, D. L. (2005), Scoring hotspots: The plume and plate paradigms, in *Plates, Plumes, and Paradigms*, edited by G. R. Foulger et al., *Geol. Soc. Am. Spec. Pap.*, *388*, 31–54.

Ding, X. M., and D. V. Helmberger (1997), Modelling D″ structure beneath Central America with broadband seismic data, *Phys. Earth Planet Inter.*, *101*(3–4), 245–270, doi: 10.1016/S0031-9201(97)00001-0.

Duffy, T. S. (2004), Earth science - Deeper understanding, *Nature*, *430*(6998), 409–410, doi:10.1038/430409a.

Flores, C., and T. Lay (2005), The trouble with seeing double, *Geophys. Res. Lett.*, *32*, L24305, doi:10.1029/2005GL024366.

Garnero, E. J. (2000), Heterogeneity of the lowermost mantle, *Annu. Rev. Earth Planet. Sci.*, *28*, 509–537, doi:10.1146/annurev.earth.28.1.509.

Garnero, E. J. (2004), A new paradigm for Earth's core-mantle boundary, *Science*, *304*(5672), 834–836, doi:10.1126/science.1097849.

Garnero, E. J., and T. Lay (1997), Lateral variations in lowermost mantle shear wave anisotropy beneath the north Pacific and Alaska, *J. Geophys. Res.*, *102*(B4), 8121–8135, doi:10.1029/96JB03830.

Garnero, E. J., and T. Lay (2003), D″ shear velocity heterogeneity, anisotropy and discontinuity structure beneath the Caribbean and Central America, *Phys. Earth Planet Inter.*, *140*(1–3), 219–242, doi:10.1016/j.pepi.2003.07.014.

Grand, S. P. (1994), Mantle shear structure beneath the Americas and surrounding oceans, *J. Geophys. Res.*, *99*(B6), 11,591–11,621, doi:10.1029/94JB00042.

Grand, S. P. (2002), Mantle shear-wave tomography and the fate of subducted slabs, *Phil. Trans. R. Soc. London, Ser. A*, *360*(1800), 2475–2491.

Grand, S. P., R. D. van der Hilst, and S. Widiyantoro (1997), Global seismic tomography: A snapshot of convection in the earth, *GSA Today*, *7*, 1–7.

He, Y. M., L. X. Wen, and T. Y. Zheng (2006), Geographic boundary and shear wave velocity structure of the "Pacific anomaly" near the core-mantle boundary beneath western Pacific, *Earth Planet. Sci. Lett.*, *244*(1–2), 302–314, doi:10.1016/j.epsl.2006.02.007.

Helmberger, D. V., and S. D. Ni (2005a), Approximate 3D body-wave synthetics for tomographic models, *Bull. Seismol. Soc. Am.*, *95*(1), 212–224, doi:10.1785/0120040004.

Helmberger, D. V., and S. D. Ni (2005b), Seismic modeling constraints on the South African Super Plume, in *Earth's Deep Mantle: Structure, Composition, and Evolution, Geophys. Monogr. Ser.*, vol. 160, edited by R. D. van der Hilst et al., pp. 65–84, AGU, Washington, D.C.

Helmberger, D. V., G. Engen, and S. Grand (1985), Upper-mantle cross-section from California to Greenland, *J. Geophys.*, *58*, 92–100.

Helmberger, D. V., T. A. Song, and D. Sun (2005), 2-D finite difference modeling of the D″ structure beneath the Eastern Cocos Plate: Part I, *Eos Trans. American Geophysical Union*, *86*(52), Fall Meet. Suppl., Abstract S34C–05.

Hernlund, J. W., and S. Labrosse (2007), Geophysically consistent values of the perovskite to post-perovskite transition Clapeyron slope, *Geophys. Res. Lett.*, *34*, L05309, doi:10.1029/2006GL028961.

Hernlund, J. W., C. Thomas, and P. J. Tackley (2005), A doubling of the post-perovskite phase boundary and structure of the Earth's lowermost mantle, *Nature*, *434*(7035), 882–886, doi:10.1038/nature03472.

Hirose, K. (2006), Postperovskite phase transition and its geophysical implications, *Rev. Geophys.*, *44*, RG3001, doi:10.1029/2005RG000186.

Hutko, A. R., T. Lay, E. J. Garnero, and J. Revenaugh (2006), Seismic detection of folded, subducted lithosphere at the core-mantle boundary, *Nature*, *441*(7091), 333–336, doi:10.1038/nature04757.

Karato, S., and B. B. Karki (2001), Origin of lateral variation of seismic wave velocities and density in the deep mantle, *J. Geophys. Res.*, *106*(B10), 21,771–21,783, doi:10.1029/2001JB000214.

Kendall, J. M., and P. M. Shearer (1994), Lateral variations in D″ thickness from long period shear-wave data, *J. Geophys. Res.*, *99*(B6), 11,575–11,590, doi:10.1029/94JB00236.

Kito, T., S. Rost, C. Thomas, and E. J. Garnero (2007), New insights into the *P*- and *S*-wave velocity structure of the D″ discontinuity beneath the Cocos plate, *Geophys. J. Int.*, *169*(2), 631–645, doi:10.1111/j.1365-246X.2007.03350.x.

Lay, T., and E. J. Garnero (2007), Reconciling the post-perovskite phase with seismological observations of lowermost mantle structure, in *Post-Perovkiste: The Last Mantle Phase Transition*, *Geophys. Monogr. Ser*, vol. 174, edited by K. Hirose et al., pp. 129–153, AGU, Washington, D. C.

Lay, T., and D. V. Helmberger (1983), A lower mantle S-wave triplication and the shear velocity structure of D, *Geophys. J. R. Astron. Soc.*, *75*(3), 799–837.

Lay, T., Q. Williams, E. J. Garnero, L. Kellogg, and M. E. Wysession (1998), Seismic wave anisotropy in the D″ region and its implications, in *The Core-Mantle Boundary Region*, *Geodyn. Ser.*, vol. 28, edited by M. Gurnis et al., pp. 299–318, AGU, Washington, D. C.

Lay, T., J. Hernlund, E. J. Garnero, and M. S. Thorne (2006), A post-perovskite lens and D″ heat flux beneath the central Pacific, *Science*, *314*(5803), 1272–1276, doi:10.1126/science.1133280.

Luo, S. N., S. D. Ni, and D. V. Helmberger (2001), Evidence for a sharp lateral variation of velocity at the core-mantle boundary from multipathed PKPab, *Earth Planet. Sci. Lett.*, *189*(3–4), 155–164, doi:10.1016/S0012-821X(01)00364-8.

Masters, G., G. Laske, H. Bolton, and A. M. Dziewonski (2000), The relative behavior of shear velocity, bulk sound speed, and compressional velocity in the mantle: Implications for chemical and thermal structure, in *Earth's Deep Interior: Mineral Physics and Tomography From the Atomic to the Global Scale*, *Geophys. Monogr. Ser.*, vol. 117, edited by S. Karato et al., pp. 63–87, AGU, Washington, D. C.

Matzel, E., M. K. Sen, and S. P. Grand (1996), Evidence for anisotropy in the deep mantle beneath Alaska, *Geophys. Res. Lett.*, *23*(18), 2417–2420, doi:10.1029/96GL02186.

Murakami, M., K. Hirose, K. Kawamura, N. Sata, and Y. Ohishi (2004), Post-perovskite phase transition in MgSiO3, *Science*, *304*(5672), 855–858, doi:10.1126/science.1095932.

Ni, S. D., X. M. Ding, and D. V. Helmberger (2000), Constructing synthetics from deep earth tomographic models, *Geophys. J. Int.*, *140*(1), 71–82, doi:10.1046/j.1365-246x.2000.00982.x.

Ni, S. D., V. F. Cormier, and D. V Helmberger (2003), A comparison of synthetic seismograms for 2D structures: Semianalytical versus numerical, *Bull. Seismol. Soc. Am.*, *93*(6), 2752–2757, doi:10.1785/0120030011.

Ohta, K., K. Hirose, T. Lay, N. Sata, and Y. Ohishi (2008), Phase transitions in pyrolite and MORB at lowermost mantle conditions: Implications for a MORB-rich pile above the core-mantle boundary, *Earth Planet. Sci. Lett.*, *267*(1–2), 107–117.

Revenaugh, J., and R. Meyer (1997), Seismic evidence of partial melt within a possibly ubiquitous low-velocity layer at the base of the mantle, *Science*, *277*(5326), 670–673, doi:10.1126/science.277.5326.670.

Russell, S. A., T. Lay, and E.J. Garnero (1998), Seismic evidence for small-scale dynamics in the lowermost mantle at the root of the Hawaiian hotspot, *Nature*, *396*(6708), 255–258, doi:10.1038/24364.

Sidorin, I., M. Gurnis, D. V. Helmberger, and X. M. Ding (1998), Interpreting D″ seismic structure using synthetic waveforms computed from dynamic models, *Earth Planet. Sci. Lett.*, *163*(1–4), 31–41, doi:10.1016/S0012-821X(98)00172-1.

Sidorin, I., M. Gurnis, and D. V. Helmberger (1999), Evidence for a ubiquitous seismic discontinuity at the base of the mantle, *Science*, *286*(5443), 1326–1331, doi:10.1126/science.286.5443.1326.

Song, T. R., and D. V. Helmberger (2007), Validating tomography model with broadband waveform modeling: Example from the La Ristra Transect in the southwestern United States, *Geophys. J. Int.*, *171*, 244–258, doi:10.1111/j.1365-246X.2007.03508.x.

Sun, D. Y., T. R. A. Song, and D. Helmberger (2006), Complexity of D″ in the presence of slab-debris and phase changes, *Geophys. Res. Lett.*, *33*, L12S07, doi:10.1029/2005GL025384.

Sun, D. Y., D. X. Song, S. H. Zheng, and D. V. Helmberger (2007a), Evidence for a chemical-thermal structure at base of mantle from sharp lateral *P* wave variations beneath Central America, *Proc. Natl. Acad. Sci. U. S. A.*, *104*(1), 26–30, doi:10.1073/pnas.0609143103.

Sun, D. Y., E. Tan, D. Helmberger, and M. Gurnis (2007b), Seismological support for the metastable superplume model, sharp features, and phase changes within the lower mantle, *Proc. Natl. Acad. Sci. U. S. A.*, *104*(22), 9151–9155, doi:10.1073/pnas.0608160104.

Tan, E., M. Gurnis, and L. J. Han (2002), Slabs in the lower mantle and their modulation of plume formation, *Geochem. Geophys. Geosyst.*, *3*(11), 1067, doi:10.1029/2001GC000238.

Thomas, C., J. Garnero, and T. Lay (2004), High-resolution imaging of lowermost mantle structure under the Cocos plate, *J. Geophys. Res.*, *109*(B8), B08307, doi:10.1029/2004JB003013.

Thomas, C., J. Wookey, and M. Simpson (2007), D″ anisotropy beneath Southeast Asia, *Geophys. Res. Lett.*, *34*, L04301, doi:10.1029/2006GL028965.

Thorne, M. S., T. Lay, E. J. Garnero, G. Jahnke, and H. Igel (2007), Seismic imaging of the laterally varying D″ region beneath the Cocos Plate, *Geophys. J. Int.*, *170*(2), 635–648, doi:10.1111/j.1365-246X.2006.03279.x.

van der Hilst, R. D. (2004), Geophysics - Changing views on Earth's deep mantle, *Science*, *306*(5697), 817–818, doi:10.1126/science.1104679.

van der Hilst, R., M. V. de Hoop, P. Wang, S.-H. Shim, P. Ma, and L. Tenorio (2007), Seismostratigraphy and thermal structure of Earth's core-mantle boundary region, *Science*, *315*(5820), 1813–1817, doi:10.1126/science.1137867.

Wang, P., M. V. deHoop, R. D. vanderHilst, P. Ma, and L. Tenorio (2006), Imaging of structure at and near the core mantle boundary using a generalized radon transform: 1. Construction of image gathers, *J. Geophys. Res.*, *111*, B12304, doi:10.1029/2005JB004241.

Wysession, M. E., et al. (1998), The D″ discontinuity and its implications, in *The Core-Mantle Boundary Region*, *Geodyn. Ser*, vol. 28, edited by M. Gurnis et al., pp. 273–297, AGU, Washington, D.C.

D. Helmberger and D. Sun, Seismological Laboratory, California Institute of Technology, 252-21, Pasadena, CA 91125, USA. (sdy@gps.caltech.edu)